UvA-DARE (Digital Academic Repository)

XENON100 Dark Matter Results from a Combination of 477 Live Days

Aprile, E.; Aalbers, J.; Breur, P.A.; Brown, A.; Colijn, A.P.; Decowski, M.P.; Tiseni, A.; XENON Collaboration

[Link to publication](#)

XENON100 dark matter results from a combination of 477 live days

E. Aprile,[1] J. Aalbers,[2] F. Agostini,[3,4] M. Alfonsi,[5] F. D. Amaro,[6] M. Anthony,[1] F. Arneodo,[7] P. Barrow,[8] L. Baudis,[8] B. Bauermeister,[9,5] M. L. Benabderrahmane,[7] T. Berger,[10] P. A. Breur,[2] A. Brown,[2] E. Brown,[10] S. Bruenner,[11] G. Bruno,[3] R. Budnik,[12] L. Bütikofer,[13] J. Calvén,[9] J. M. R. Cardoso,[6] M. Cervantes,[14] D. Cichon,[11] D. Coderre,[13] A. P. Colijn,[2] J. Conrad,[9,*] J. P. Cussonneau,[15] M. P. Decowski,[2] P. de Perio,[1,†] P. Di Gangi,[4] A. Di Giovanni,[8] S. Diglio,[15] E. Duchovni,[12] J. Fei,[16] A. D. Ferella,[9] A. Fieguth,[17] D. Franco,[8] W. Fulgione,[3,18] A. Gallo Rosso,[3] M. Galloway,[8] F. Gao,[16] M. Garbini,[4] C. Geis,[5] L. W. Goetzke,[1] Z. Greene,[1] C. Grignon,[5] C. Hasterok,[11] E. Hogenbirk,[2] R. Itay,[12] B. Kaminsky,[13] G. Kessler,[8] A. Kish,[8] H. Landsman,[12] R. F. Lang,[14] D. Lellouch,[12] L. Levinson,[12] M. Le Calloch,[15] C. Levy,[10] Q. Lin,[1] S. Lindemann,[11] M. Lindner,[11] J. A. M. Lopes,[6,‡] A. Manfredini,[12] T. Marrodán Undagoitia,[11] J. Masbou,[15] F. V. Massoli,[4] D. Masson,[14] D. Mayani,[8] Y. Meng,[19] M. Messina,[1] K. Micheneau,[15] B. Miguez,[18] A. Molinario,[3] M. Murra,[17] J. Naganoma,[20] K. Ni,[16] U. Oberlack,[5] S. E. A. Orrigo,[6,§] P. Pakarha,[8] B. Pelssers,[9] R. Persiani,[15] F. Piastra,[8] J. Pienaar,[14] M.-C. Piro,[10] G. Plante,[1] N. Priel,[12] L. Rauch,[11,‖] S. Reichard,[14] C. Reuter,[14] A. Rizzo,[1] S. Rosendahl,[17] N. Rupp,[11] J. M. F. dos Santos,[6] G. Sartorelli,[4] M. Scheibelhut,[5] S. Schindler,[5] J. Schreiner,[11] M. Schumann,[13] L. Scotto Lavina,[15] M. Selvi,[4] P. Shagin,[20] M. Silva,[6] H. Simgen,[11] M. v. Sivers,[13] A. Stein,[19] D. Thers,[15] A. Tiseni,[2] G. Trinchero,[18] C. D. Tunnell,[2] R. Wall,[20] H. Wang,[19] M. Weber,[1] Y. Wei,[8] C. Weinheimer,[17] J. Wulf,[8] and Y. Zhang[1]

(XENON Collaboration)[¶]

[1]*Physics Department, Columbia University, New York, New York 10027, USA*
[2]*Nikhef and the University of Amsterdam, Science Park, Amsterdam 1098XG, Netherlands*
[3]*INFN-Laboratori Nazionali del Gran Sasso and Gran Sasso Science Institute, L'Aquila 67100, Italy*
[4]*Department of Physics and Astrophysics, University of Bologna and INFN-Bologna, Bologna 40126, Italy*
[5]*Institut für Physik & Exzellenzcluster PRISMA, Johannes Gutenberg-Universität Mainz, Mainz 55099, Germany*
[6]*Department of Physics, University of Coimbra, Coimbra 3004-516, Portugal*
[7]*New York University Abu Dhabi, Abu Dhabi, United Arab Emirates*
[8]*Physik-Institut, University of Zurich, Zurich, Switzerland*
[9]*Oskar Klein Centre, Department of Physics, Stockholm University, AlbaNova, SE-106 91 Stockholm, Sweden*
[10]*Department of Physics, Applied Physics and Astronomy, Rensselaer Polytechnic Institute, Troy, New York 12180, USA*
[11]*Max-Planck-Institut für Kernphysik, Heidelberg 69117, Germany*
[12]*Department of Particle Physics and Astrophysics, Weizmann Institute of Science, Rehovot, Israel*
[13]*Albert Einstein Center for Fundamental Physics, University of Bern, Bern 3012, Switzerland*
[14]*Department of Physics and Astronomy, Purdue University, West Lafayette, Indiana 47907, USA*
[15]*SUBATECH, Ecole des Mines de Nantes, CNRS/In2p3, Université de Nantes, Nantes 44307, France*
[16]*Department of Physics, University of California, San Diego, California, USA*
[17]*Institut für Kernphysik, Wilhelms-Universität Münster, Münster 48149, Germany*
[18]*INFN-Torino and Osservatorio Astrofisico di Torino, Torino 10125, Italy*
[19]*Physics & Astronomy Department, University of California, Los Angeles, California 90095, USA*
[20]*Department of Physics and Astronomy, Rice University, Houston, Texas 77005, USA*

We report on WIMP search results of the XENON100 experiment, combining three runs summing up to 477 live days from January 2010 to January 2014. Data from the first two runs were already published. A blind analysis was applied to the last run recorded between April 2013 and January 2014 prior to combining the results. The ultralow electromagnetic background of the experiment, $\sim 5 \times 10^{-3}$ events/(keV$_{ee}\times$ kg $\times$ day)) before electronic recoil rejection, together with the increased exposure of 48 kg $\times$ yr, improves the sensitivity. A profile likelihood analysis using an energy range of (6.6–43.3) keV$_{nr}$ sets a limit on the elastic, spin-independent WIMP-nucleon scattering cross section for WIMP masses above 8 GeV/c^2, with a

*Wallenberg Academy Fellow.
†pdeperio@astro.columbia.edu
‡Also at Coimbra Engineering Institute, Coimbra, Portugal.
§Present address: IFIC, CSIC-Universidad de Valencia, Valencia, Spain.
‖rauch@mpi-hd.mpg.de
¶xenon@lngs.infn.it

122001-1

minimum of 1.1×10^{-45} cm^2 at 50 GeV/c^2 and 90% confidence level. We also report updated constraints on the elastic, spin-dependent WIMP-nucleon cross sections obtained with the same data. We set upper limits on the WIMP-neutron (proton) cross section with a minimum of 2.0×10^{-40} cm^2 (52×10^{-40} cm^2) at a WIMP mass of 50 GeV/c^2, at 90% confidence level.

I. INTRODUCTION

Astrophysical observations at various scales give strong evidence for the existence of a nonluminous (rarely interacting), nonbaryonic, and nonrelativistic (cold) matter component that makes up 27% of the total mass-energy budget of the Universe, consisting of yet undetected particles whose nature remains unknown [1,2]. Many theories beyond the Standard Model of particle physics predict possible candidates, the most promising of which are weakly interacting massive particles (WIMPs) [3,4]. In this paradigm, WIMPs would interact with target nuclei of detectors placed deeply underground, shielded by the rock overburden, inducing detectable nuclear recoil (NR) signals.

A plethora of experiments worldwide are devoted to observing the low-energy NRs of a few keV induced by WIMPs scattering off a nucleus [5]. Among these, the XENON100 experiment exploits a dual-phase (liquid-gas) xenon time projection chamber (TPC) [6]. An electric "drift" field of ~500 V/cm is applied across the liquid xenon (LXe) volume by quasitransparent electrodes (meshes); a stronger electric "extraction" field of ~12 kV/cm is applied in the gaseous xenon (GXe) multiplication region above the liquid-gas interface.

Particles interacting in LXe create a scintillation light signal (S1) that is directly measured by 178 Hamamatsu R8520-AL photomultiplier tubes (PMTs), as well as ionization electrons that can escape the local ionization field and migrate along the drift field direction towards the top of the TPC. Those ionization electrons that reach the liquid-gas interface are extracted into the GXe and accelerated by the extraction field, producing a scintillation signal (S2) that is proportional to the number of extracted ionization electrons. The S1 and S2 signal timing and S2 hit pattern are used to determine the X,Y,Z coordinates of an interaction [6]. This event-by-event 3D-position information can be used to define an optimal fiducial volume to increase the signal to background ratio.

The XENON100 detector [6] features an active dark matter target of 62 kg and is installed at the Laboratori Nazionali del Gran Sasso (LNGS, Italy). Careful material selection [7] and detector design lead to very low backgrounds from electronic (ER) [8] and nuclear recoils (NR) [9]. During the operation period between 2009 and 2016, three science runs (dark matter data sets) were collected. The results of the first two runs, referred to as run I (100.9 live days in 2010) [10,11] and run II (224.6 live days during 2011 and 2012) [12,13] were published and provided the

best constraints on the spin-independent as well as on the spin-dependent WIMP-neutron cross section at the time of publication. The final run (run III) was taken between 2013 and 2014 (153.6 live days) and its results are published here for the first time in combination with the other two runs.

In this work, several improvements to the analysis and statistical interpretation are discussed in Sec. II. The results of the spin-independent (SI) and spin-dependent (SD) combined analysis of all 477 live days of XENON100 dark matter science data are presented in Sec. III.

II. WIMP SEARCH DATA ANALYSIS

This paper includes the reanalysis of run I and run II data and the first analysis of run III data, where each run corresponds to a data set with different detector settings and background levels. This section describes the general analysis procedure common to all three runs, emphasizing the modifications to the procedure reported in [14]. Section II A defines the energy scale for NRs. Section II B describes the operational differences between the three runs and run-dependent detector quantities. A detailed description of the data selection criteria and signal acceptance follows in Secs. II C and II D, respectively. The signal and background models are discussed in Secs. II E and II F. In Sec. II G, the likelihood function used for the final statistical inference is described.

A. Energy scale

For a given energy deposition, the scintillation photons that reach the PMT photocathode may create photoelectrons (PEs) that are then amplified within the PMT. The probability of detecting such scintillation photons is, among other effects [6], dependent on the interaction position due to changing solid angles with respect to the PMT arrays. Hence, a light collection efficiency (LCE) correction, dependent on the position, needs to be applied to the signal in order to achieve a uniform detector response at a given energy. The corrected signal (cS1) represents a spatially uniform response in the detector. Similarly, the measured S2 signal has a spatial dependence on the position both in the horizontal plane mainly due to warping of the top meshes [6] and in the vertical direction because of the finite electron lifetime caused by electronegative impurities in the LXe. Both effects can be quantified to achieve a position corrected signal, cS2. More details on signal corrections are provided elsewhere [6].

TABLE I.   Detector and analysis parameters considered in each run.

		Run I	Run II	Run III
Science campaign	Live days (d)	100.9	223.1	153.0
	Period	2010	2011–2012	2013–2014
Detector condition	Average electron lifetime (μs)	294 ± 37	519 ± 64	720 ± 110
	L_y (PE/keV)	2.20 ± 0.09	2.28 ± 0.04	2.25 ± 0.03
	S2 amplification (PE/e$^-$)	18.6 ± 6.6	19.6 ± 6.9	17.1 ± 6.4
	Extraction field in gas (kV/cm)	11.89 ± 0.02	10.30 ± 0.01	11.50 ± 0.02
	Drift field (V/cm)	533	533	500
Calibration	^{60}Co, ^{232}Th ER calibration in S1 range (events)	4116	15337	10469
	^{241}AmBe NR calibration in S1 range (events)	55423	25315	92226
Analysis	Low S1 threshold (PE)	3	3	3
	High cS1 threshold (PE)	30	30	30
	Low S2 threshold (PE)	300	150	150
	Fiducial mass (kg)	48	34	34
	Total selected sample (events)	929	402	346
	Expected background in benchmark ROI (events)	3.9 ± 0.5	1.7 ± 0.3	1.0 ± 0.2
	Candidates in benchmark ROI (events)	3	1	1

The S1 and S2 signals provide information on the energy released by particles interacting in LXe. In this analysis, nuclear recoil processes are of greatest interest. For the direct scintillation signal, the relationship between the nuclear recoil energy E_{nr} and cS1 is given by (see [15] and references therein)

$$E_{nr} = \frac{cS1}{L_y} \frac{1}{\mathcal{L}_{eff}(E_{nr})} \frac{S_{ee}}{S_{nr}}, \quad (1)$$

where $S_{ee} = 0.58$ and $S_{nr} = 0.95$ describe the scintillation quenching due to the electric field [16], L_y is the detector-dependent light yield at 122 keV$_{ee}$ (electron recoil equivalent energy) shown in Table I, and $\mathcal{L}_{eff}$ is the LXe relative scintillation efficiency. The parametrization and uncertainties of $\mathcal{L}_{eff}$ as a function of E_{nr} are based on existing direct measurements [10].

For the S2 signal, the energy scale is given by (see [17] and references therein)

$$E_{nr} = \frac{cS2}{Y} \frac{1}{Q_y(E_{nr})}, \quad (2)$$

where the secondary amplification factor Y is determined from the detector response to single electrons [18] and the parametrization of $Q_y(E_{nr})$ is taken from [17]. The corrected S2 observed by the bottom PMT array, cS2$_b$, is used for the following analysis. In contrast to previous publications [10,12], where the signal model was only modeled in S1, this analysis also incorporates the calculated S2 distribution based on the accurate simulation of the secondary scintillation signal of NRs [17].

B. Detector operation

Science data taken with different detector conditions must be corrected individually to avoid large systematic uncertainties. Therefore, the corrections for the measured quantities in each run are treated separately and the relevant differences are outlined below and summarized in Table I.

For the analysis of the combined data, the light yield at 122 keV$_{ee}$ does not change significantly among the different data sets. The S2 signal corrections are treated individually in each run. In particular the average electron lifetime increases from an average of (294 ± 37) μs in run I to an average of (720 ± 110) μs in run III, while the exact time evolution during the runs is used in the correction. Small differences of a few ± 100 V in the anode voltage and in liquid level result in different S2 amplification factors as shown in Table I. The gain values for the PMTs are monitored on a weekly basis and an average value over the data taking period of each run is used. The ^{nat}Kr concentration is larger in run I (360 ± 70) ppt [10] compared to run II (19 ± 4) ppt [12] and III (6 ± 1) ppt. It is measured, similarly to [12], in extracted GXe samples from the detector using ultrasensitive rare gas mass spectrometry [19].

The detector response to NR and ER is characterized by a ^{241}AmBe (α, n) source and ^{137}Cs, ^{60}Co, ^{232}Th γ-sources, respectively [6]. The ^{241}AmBe source and low energy Compton tail of the high-energy γ-sources, ^{60}Co and ^{232}Th, are used to determine the signal acceptances of the event selection. The latter is also used to model the background events caused by β- and γ-particles. The total number of events for each calibration run after applying the selection described below is shown in Table I.

C. Data selection

The event selection criteria for identifying single scatter events are described in previously published results [10,12] as well as in a detailed publication on the analysis of the XENON100 data [14]. For this analysis, there is no change

to the selection for run I. However, in addition to the already presented event selection for run II, a few post-unblinding cuts were developed to improve data quality and signal purity, described below. For run III, due to similar detector conditions, the criteria from run II were adopted and tuned while blinding the dark matter data in the relevant energy range.

An analysis of the lone-S1 (an S1 without any correlated S2) rate over time revealed periods of significantly higher rates corresponding to a nonrandom occurrence of S1s. This increases the probability of an accidental coincidence with a lone random S2 in those periods, which could mimic the signature of a dark matter candidate event. The exact cause of this effect is not known, but is indicative of unusual detector behavior and these time periods were excluded from the analysis. This new data quality criterion was optimized with the lone-S1 sample of the run II dark matter data, removing data periods where three or more lone S1s are present in a 500 second window. This data quality criterion was applied postunblinding to all runs. The optimization procedure, however, was fixed based on run II. This criterion reduces the live times of runs II and III by 1.5 d and 0.6 d, respectively, and excludes one event from the run II benchmark region as shown in Fig. 1. No such high rate periods were found in run I.

A second novel selection criterion was determined from an improved S1 and S2 classification algorithm [20], initially developed for the next-generation experiment XENON1T [21]. The new algorithm improves the identification of single electron S2s [18], which the default XENON100 algorithm sometimes misidentifies as an S1. This new criterion has been applied postunblinding to run II and blinded to run III dark matter data, reducing the expected non-Gaussian background (described in Sec. II F) by ~63% with a signal acceptance of >98% across the energy region of interest.

For a 100% S2-trigger efficiency in run I, the threshold on the minimum amplitude of the proportional scintillation signal was set to $S2 > 300$ PE since the trigger roll off begins at 280 PE (see Fig. 2 of [14]). Due to a lower trigger threshold in runs II and III, the S2 threshold condition was improved to $S2 > 150$ PE. The S1 threshold is now equalized for all runs to $S1 > 3$ PE, while an upper limit of the S1 range is set on the corrected signal to $cS1 < 30$ PE. Since the probability to detect a signal depends on the number of photons produced at the interaction site prior to LCE corrections, using S1 instead of cS1 for the low energy threshold is a more proper treatment, which is especially important towards very low energies. This results in a variable energy threshold as shown in Fig. 2 where regions of the TPC with a higher LCE close to the bottom PMT array exhibit a smaller energy threshold 3 keV_{nr} (nuclear recoil equivalent energy), while the top region of the fiducial volume requires a minimum energy deposition of 8.5 keV_{nr}. The
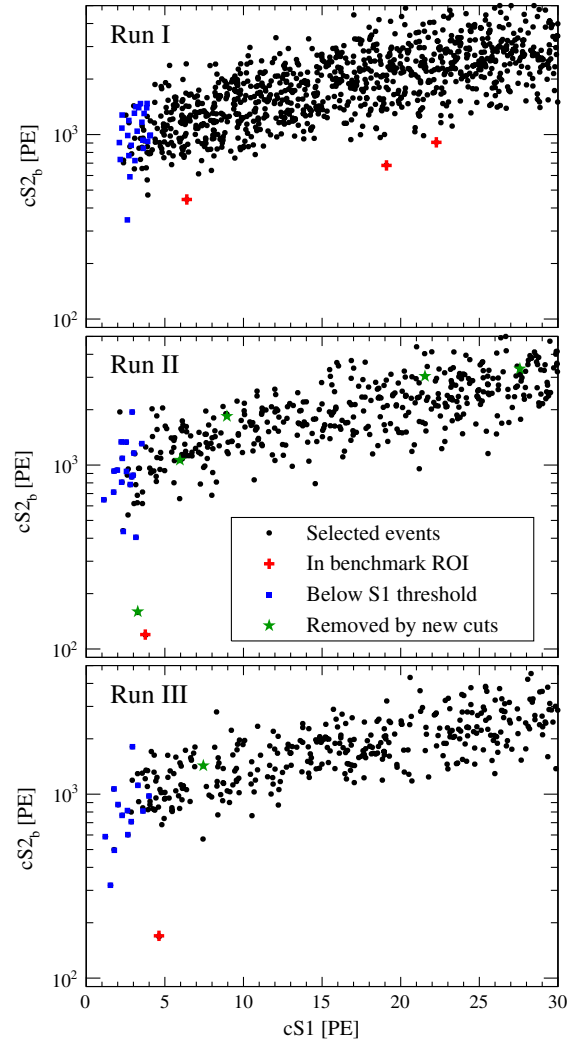

FIG. 1.   The cS1 and $cS2_b$ for runs I (top), II (middle), and III (bottom) science data passing all selection criteria (black circles, with red crosses for dark matter candidates in the ROI). Events that fall below the S1 threshold (blue squares) are not used in the analysis. Events that were removed by the new high S1 rate and improved S2 classification cuts are also shown (green stars). The total number of events is summarized in Table I.

relation between S1 and cS1, after applying the LCE correction, and the corresponding thresholds are shown in Fig. 3.

The final dark matter candidate samples after selection are shown in Fig. 1 for runs I, II, and III, where the events removed by the new selection criteria are highlighted. The y-axes of the plots are shown in units of the corrected S2 signal in the bottom array only ($cS2_b$). A benchmark region of interest (ROI) can be defined similarly to [14] after all selection criteria, between the upper and lower thresholds in cS1 and S1 as stated in Table I. This ROI is bounded in $cS2_b/cS1$ discrimination space above by the 99.75% ER rejection line and below by the lower 3σ quantile of the AmBe neutron calibration data.
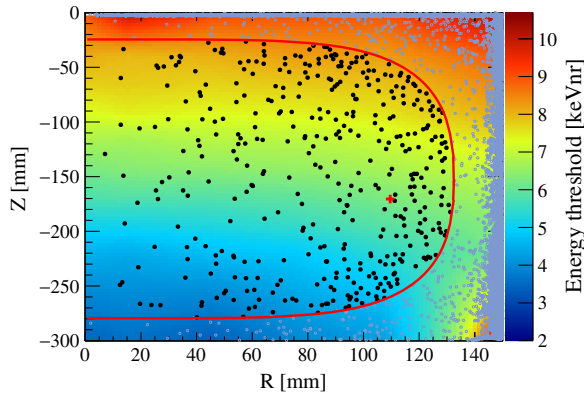
FIG. 2.   The varying energy threshold in keV$_{nr}$ due to the new threshold in S1, inside the active volume of the TPC as a function of the radius, R, and depth, Z. The color scale is a mapping of the LCE and S1 = 3 PE to energy assuming average values of $\mathcal{L}_{eff}$ and Q_y. The run III data inside (solid black points, with red cross for the candidate in the ROI) and outside (hollow gray points) the fiducial volume (red line) are shown.

D. Signal acceptance

The signal acceptance is estimated similarly to [14] by defining a control sample from calibration data using all the selection criteria (cuts) except the one whose acceptance is to be estimated. NR calibration data are used for most of the cuts, while cuts that are more susceptible to noise (S1 coincidence and electronic noise cuts [14]) use ER calibration data, which span more of the science data taking runs.

The acceptance for a given cut is evaluated as a function of the primary parameter used in that cut, for example cS1 for the single S1 cut or cS2 for the S2 width cut. The acceptance of the S1 coincidence cut, previously a function of cS1 as in Fig. 3 of [14], was found to vary by up to 15% with changing LCE. Thus, we now parametrize this acceptance as a function of S1 instead.
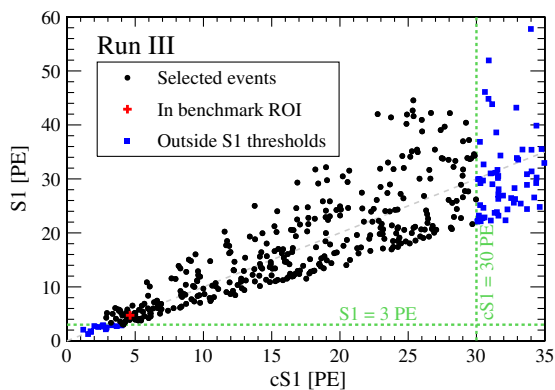

FIG. 3.   The S1 and cS1 derived from the LCE for the run III data. Events below the lower S1 threshold at S1 = 3 PE (horizontal line) and above the upper threshold at 30 PE in cS1 (vertical line) are removed from the analysis (blue squares). The S1 = cS1 line is shown for reference. The dark matter candidate in the ROI is highlighted (red cross).

This analysis selects the primary S1 as that with the most PMT coincidences in a waveform. However, correlated electronic noise can be misidentified as the primary S1 and contaminate an event with a real signal, causing the event to be removed from the control samples and underestimating the acceptances. The acceptance loss is now estimated from the probability that a noisy peak accompanying a good S1 peak in an event is misidentified as the primary S1. Figure 4 (top) shows this new noise misidentification acceptance
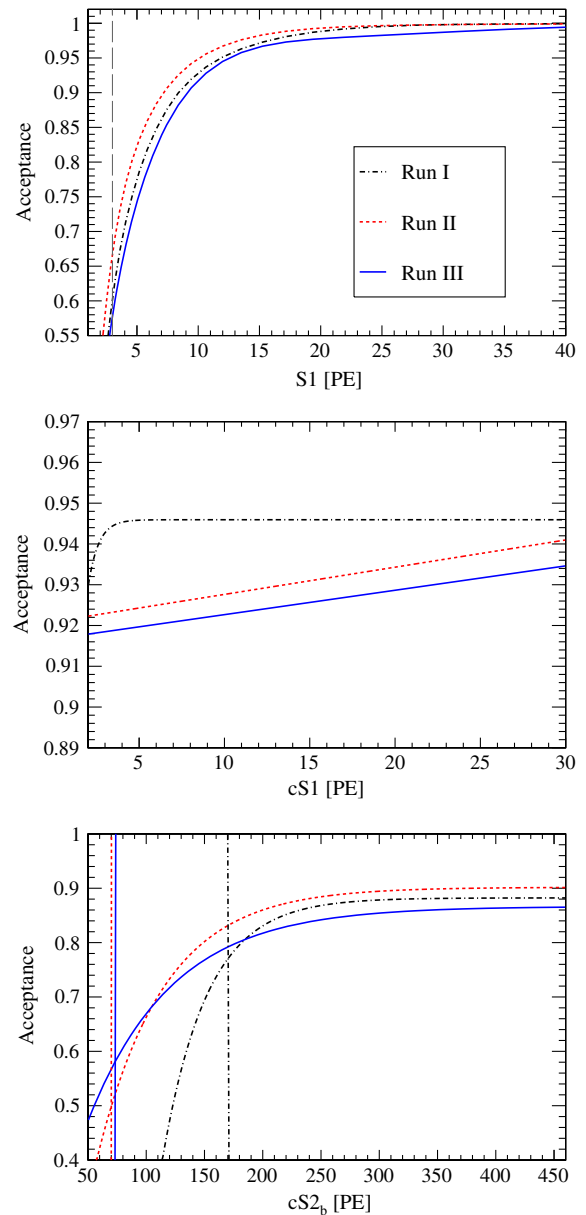

FIG. 4.   The combined acceptance of the S1 coincidence cut and noise misidentification (top), and the cumulative acceptance of the rest of the cS1-based cuts (middle) and cS2-based cuts (bottom), for each science run. The acceptance in cS2 is constant above 450 pe. The S2 thresholds for each run are indicated by the vertical lines.

loss, combined with the S1 coincidence cut acceptance, as a function of S1.

The same procedure is applied across all three science runs and the cumulative acceptance of all the cuts in each parameter space is shown in Fig. 4. The small differences between runs are due to the varying detector parameters and cut optimization. The total uncertainty is estimated to be less than 20% based on differences in ^{241}AmBe or ER calibration data and the selection of the control samples. This increases the profile likelihood limit by a negligible few percent and is hence not considered as a nuisance parameter. The acceptances of the S1, cS1 and S2 thresholds are taken into account by applying these cuts directly on the signal model, which is described in the following section.

E. Signal model

The signal model describing the rate of WIMP interactions, R, in the detector is given by [22]

$$\frac{dR(m_\chi, \sigma)}{dE} = \frac{\rho_0}{m_\chi \cdot m_A} \cdot \int v \cdot f(v) \cdot \frac{d\sigma}{dE}(E, v) d^3 v, \quad (3)$$

where E is E_{nr} in Eqs. (1) and (2); $\rho_0 = 0.3 \text{ GeV/cm}^3$ is the local dark matter density [23]; m_χ and m_A are the WIMP and nucleus mass, respectively; and $f(v)$ is the distribution of dark matter particle velocities v. An isothermal WIMP halo is assumed for $f(v)$ with an escape velocity of $v_{esc} = 544 \text{ km/s}$ [24] and a local circular velocity of $v_0 = 220 \text{ km/s}$. The differential cross section, $\frac{d\sigma}{dE}$, is composed of a SI and SD contribution [22]:

$$\frac{d\sigma}{dE} = \frac{m_A}{2\mu_A^2 v^2} \cdot (\sigma_{SI} F_{SI}^2(E) + \sigma_{SD} F_{SD}^2(E)), \quad (4)$$

where μ_A is the reduced mass of the nucleus and WIMP, and F and σ are the Helm form factors [22] and cross sections as $q \to 0$, respectively, for SI and SD interactions described in the following sections. Each component is considered separately in the profile likelihood (PL) analysis below, with the other one being fixed to zero.

The rate as a function of detector observables can then be written following [10] as

$$\frac{d^2 R(m_\chi, \sigma; \mathcal{L}_{eff}, \text{LCE}, Q_y)}{d(cS1)d(cS2_b)} \approx \epsilon(S1)\epsilon(cS1)\epsilon(cS2_b)$$

$$\times \int \frac{dR}{dE} p(cS1|E, \mathcal{L}_{eff}, \text{LCE})$$

$$\times p(cS2_b|E, Q_y) dE, \quad (5)$$

where $\epsilon(S1)$, $\epsilon(cS1)$, and $\epsilon(cS2_b)$ are the acceptances shown in Fig. 4, and p denotes the probability distribution functions (PDFs) to observe cS1 or cS2$_b$ given a recoil energy, E [12]. The approximation assumes a

negligible anticorrelation between S1 and S2 signals for NRs, as suggested by [17], such that the acceptances and probabilities can be multiplied independently as $p(cS1, cS2) \approx p(cS1) \cdot p(cS2)$. Finally, the lower thresholds in S1 and S2 are applied directly to the computed spectra, which can then be integrated to estimate the total number of expected signal events:

$$N_s(m_\chi, \sigma, \mathcal{L}_{eff}, \text{LCE}, Q_y)$$

$$= \int_{cS1=0}^{30} \int_{cS2_b=0}^{cS2_b^{up}} \frac{d^2 R}{d(cS1)d(cS2_b)} d(cS1)d(cS2_b), \quad (6)$$

where cS2$_b^{up}$ is an upper bound that includes the whole ER band. The signal shape is given by the following PDF:

$$f_s(cS1, cS2_b; m_\chi, \mathcal{L}_{eff}, \text{LCE}, Q_y) = \frac{1}{N_s} \frac{d^2 R}{d(cS1)d(cS2_b)}. \quad (7)$$

To account for uncertainties in the PL analysis below, the spectra are computed for each run, WIMP mass, LCE and values of $\mathcal{L}_{eff}$ and Q_y.

Following a similar procedure as in [25] the (cS1, cS2$_b$) spectra are binned into 8 bands, with equal numbers of signal events in the nominal model, to exploit the knowledge of the signal shape and allow the statistical interpretation in regions with optimal signal to background ratios. The lower bound is defined by the 99.7% acceptance line of the 20 GeV/c^2 WIMP signal model to keep the selected signal events for all WIMP masses fixed. The upper bound is defined by cS2$_b^{up}$ in Eq. (6). Two examples of the banding are shown in Fig. 5.
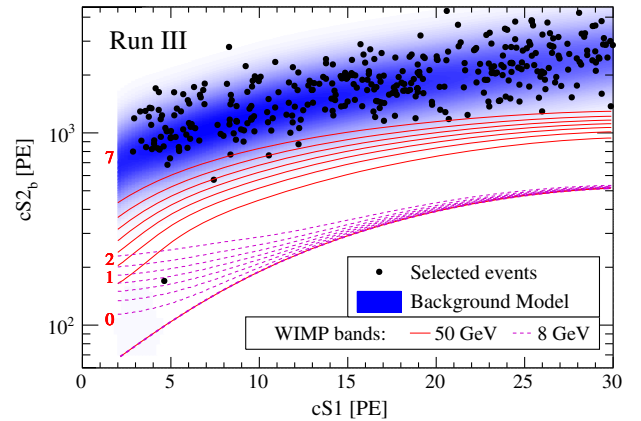

FIG. 5. Example bands for 8 GeV/c^2 (purple dashed lines) and 50 GeV/c^2 (red solid lines with numbered labels) WIMP mass SI signal models. The lower bound for all WIMP masses is defined by the 20 GeV/c^2 model as described in the text. The upper bound of the topmost band is beyond the vertical range. The shape of the background model is shown with a (blue) linear color scale. The run III science data are overlaid for reference.

1. *Spin-independent cross section*

By assuming a spin-independent and isospin conserving interaction, the cross section can be computed as

$$\sigma_{SI} = \sigma_p \cdot \frac{\mu_A^2}{\mu_p^2} \cdot A^2, \qquad (8)$$

where σ_p is the WIMP-proton cross section, A is the nucleus mass number and μ_p is the reduced mass of the proton and WIMP. Examples of corresponding computed spectra for each run are shown in Fig. 6. The green line in the top panel of Fig. 6 is the energy spectrum as given by Eqs. (3) and (8) for an 8 GeV/c^2 WIMP. The observable cS1 and cS2$_b$ spectra from Eq. (5) are also shown for each run, illustrating that for low WIMP masses, Poisson fluctuations of the generated signal quanta are essential to observe signals above the energy threshold of the detector.

2. *Spin-dependent cross section*

Following the work of [13], a combination of the three science runs can also strengthen the dark matter spin-dependent interaction results. The corresponding structure functions are based on a chiral effective field

FIG. 6. Expected rate in cS1 (top) and cS2$_b$ (bottom) of an 8 GeV/c^2 WIMP SI signal and a cross section of 1×10^{-44} cm^2 for each science run. The initial energy spectrum in keV$_{nr}$ is shown (green long-dashed). The average LCE = 1 is shown, for example, resulting in the hard cut at S1 = cS1 = 3 PE. The S2 thresholds for each run are indicated by the vertical lines. The differences in the spectra are due to varying exposures, S2 threshold, and acceptances.

theory considering two body currents as computed in [26], resulting in the following cross section:

$$\sigma_{SD} = \frac{32}{\pi} \mu_A^2 \cdot G_F^2 [a_p \langle S_p \rangle + a_n \langle S_n \rangle]^2 \cdot \frac{J+1}{J}, \qquad (9)$$

where G_F is the Fermi coupling constant, J is the total nuclear spin, $a_{p,n}$ are the effective proton and neutron couplings, and $\langle S_{p,n} \rangle$ is the expectation of the total nuclear spin operator.

F. Background model

This section describes how the ER and NR backgrounds are modeled and combined into a total background model. These are derived similarly to the run II method in [12] with the addition of a new method to model the accidental coincidence component of the ER non-Gaussian background.

The NR background model is estimated by Monte Carlo simulation [9], including a radiogenic component, f_{RG}^{NR}, from ambient materials and a cosmogenic component, f_{CG}^{NR}, from cosmic radiation and their secondary processes. The computed energy spectra are translated to cS1 and cS2$_b$ following the procedure in the previous Sec. II E and normalized to the exposure of each run. The total NR background prediction is then $f^{NR} = f_{RG}^{NR} + f_{CG}^{NR}$, where the functional dependence on cS1 and cS2 is suppressed for brevity, and shown in Fig. 7 (bottom).

The ER background consists of a Gaussian-shaped component and a non-Gaussian component. The Gaussian component, f_G^{ER} shown in Fig. 7 (top), is modeled as in [12] by parametrizing the ER calibration data from each run and normalizing to the dark matter data above the ROI.

The non-Gaussian component consists of anomalous events, such as those that show incomplete charge collection and accidental coincidences (AC) of lone (uncorrelated) S1s and S2s. Previously [12], these events were effectively modeled by a parametrization, f_{AN}^{ER}, of ER calibration events in the ROI after subtraction of the Gaussian component. However, this model is underestimating the effect of the AC contribution. Hence, a more physically motivated procedure considering both non-Gaussian contributions is used to derive the background model. The new AC component model, described in the Appendix, identifies high statistics samples of lone S1s and S2s to estimate this background with a better understanding of the spectral shape. The product of the rates of these two samples gives the AC rate. Distinct AC rates for both the ER calibration data, f_{AC}^{ER}, and dark matter data, f_{AC}^{DM}, can be derived using this method. The prediction for ER calibration data is consistent with the observed number of events in the ROI, validating the model. The total non-Gaussian model is then given by $f_{NG}^{ER} = f_{AC}^{DM} + \max(f_{AN}^{ER} - f_{AC}^{ER}, 0)$, where the last term describes any remaining part of the anomalous leakage that is not accounted for by accidental

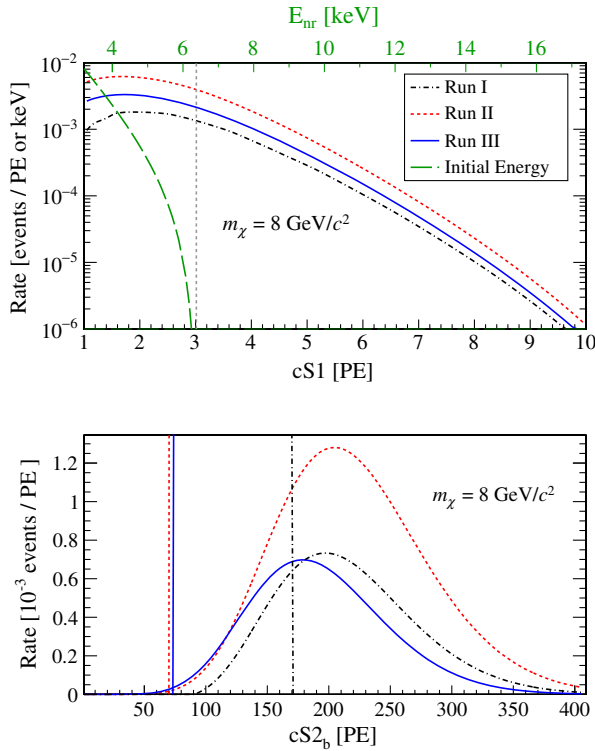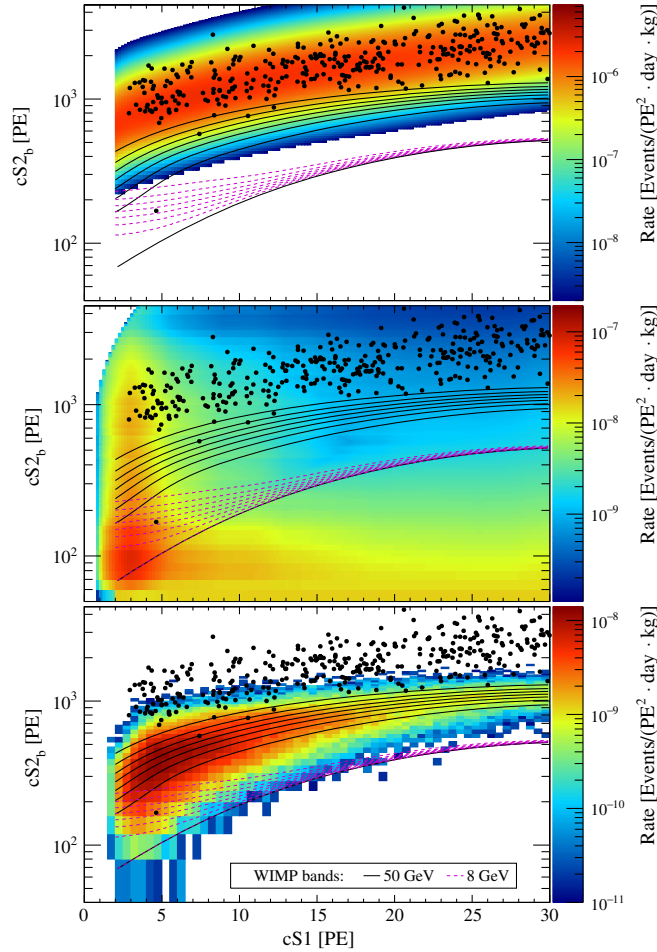FIG. 7. The ER Gaussian (top), non-Gaussian ER (middle), and NR (bottom) background predictions for Run III. The science data and signal bands, as in Fig. 5, are overlaid for reference.

FIG. 8. Expected event rates for PL band 0 (top) and 2 (bottom) from Fig. 5 for a 50 GeV/c^2 WIMP and an assumed SI cross section of $\sigma_{\mathrm{SI}} = 10^{-45}$ cm^2 (long-dashed magenta line). The contribution from various background components described in the text (nonsolid colored lines) are shown together with their sum (solid black line). The non-AC component of the total non-Gaussian ER background is shown (diagonal line filled area). The run III models are shown for example and the cS1 of the ROI event is shown on the horizontal axis (blue point).

coincidences. This model is shown in Fig. 7 (middle), where the bulk at low S1 is dominated by the AC component, whereas the tail towards high S1 can be explained by the non-AC anomalous leakage component. The contribution of each component is shown for two example PL bands in Fig. 8.

Finally, the total background model is given by

$$f_b = f^{\mathrm{NR}} + f_G^{\mathrm{ER}} + f_{\mathrm{NG}}^{\mathrm{ER}}, \qquad (10)$$

for each run, shown in Fig. 5 for run III. The projection in cS1 for two example bands is shown in Fig. 8 including the contribution from each background component. The integrated event rate for each PL band is shown in Fig. 9 and the fractional contributions to the ROI for each run are shown in Table II. Run I is ^{85}Kr dominated which results in a smaller relative contribution of the NR background in comparison to runs II and III. The non-Gaussian data-driven model predicts a smaller contribution in run III compared to run II. A sideband unblinding of the run III science data around the ROI was performed similarly to
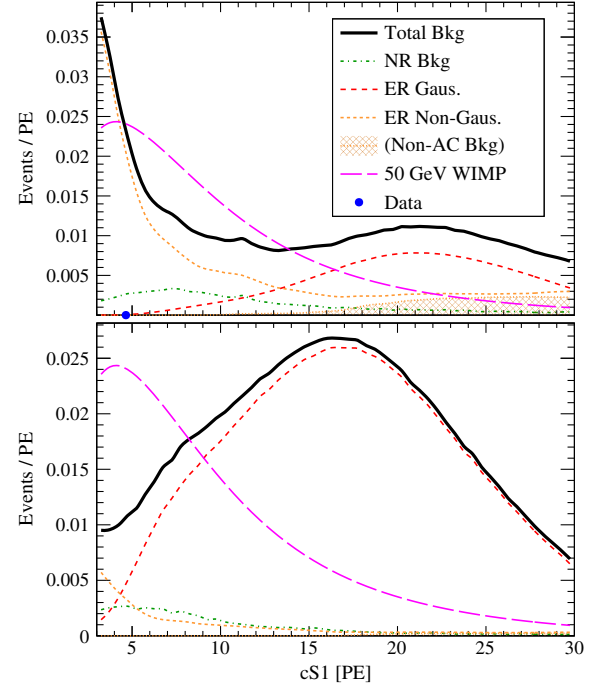
run II [14] to test and validate the background models. No significant deviations from the predictions were found.

The previous PL analysis [25] assumed an effective uncertainty on the total background model by including a Poisson constraint term based on the number of ER calibration events in each band [Eq. (14) below]. This uncertainty is now cross-checked by propagating the systematic errors for each background component, including errors from the parametrization fits to calibration data, selection criteria and efficiency uncertainties for the AC model, and muon flux normalization uncertainty for the NR component. The total error for each background component and their quadrature sum is shown in Fig. 10. The Poisson error is chosen for this analysis as it conservatively overestimates the propagated errors, which may be overconstrained from the assumed (nonphysical) parametrizations.

G. The likelihood function

The signal hypothesis test is performed by means of a profiled likelihood ratio test statistic and its asymptotic distributions [27]. The procedure is described in detail in [25] and only the modifications for this analysis are highlighted here.
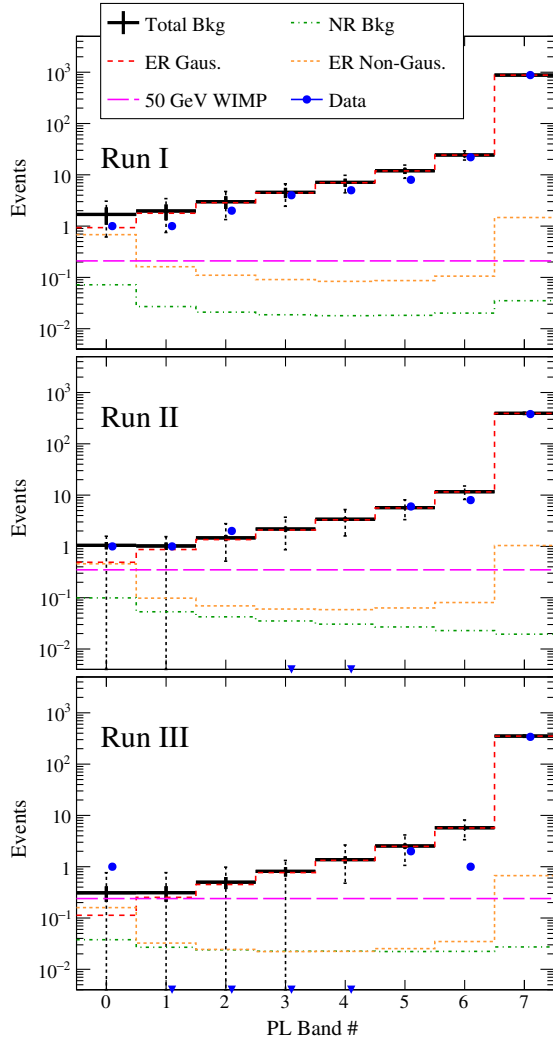
$$\mathcal{L}^i = \mathcal{L}_1^i(m_\chi; \sigma, N_b^i, \boldsymbol{\epsilon_b^i}, t_{\mathcal{L}_{\text{eff}}}, t_{Q_y}) \times \mathcal{L}_2^i(\boldsymbol{\epsilon_b^i}), \quad (12)$$

where $\boldsymbol{\epsilon_b^i}$ indicates a vector of the background nuisance parameter per band j and

$$\mathcal{L}_1^i = \prod_j^{K^i(m_\chi)} \text{Poiss}(n^{i,j}|\epsilon_s^{i,j} N_s^i(\sigma) + \epsilon_b^{i,j} N_b^i)$$

$$\times \prod_{k=1}^{n^{i,j,k}} \frac{\epsilon_s^{i,j} N_s^i(\sigma) f_s^{i,j}(\text{cS1}^k) + \epsilon_b^{i,j} N_b^i f_b^{i,j}(\text{cS1}^k)}{\epsilon_s^{i,j} N_s^i(\sigma) + \epsilon_b^{i,j} N_b^i} \quad (13)$$

is the extended likelihood function. The number of observed events is $n^{i,j}$, and N_s^i and N_b^i are the maximum likelihood estimators (MLEs) for the total number of signal and background events, respectively. The ROI is divided into 8 bands, $K^i(m_\chi)$, depending on the WIMP mass as depicted in Fig. 5. The fractions, $\epsilon_{s,b}^{i,j}$, for each band are derived from the signal and background models. $N_s^i(\sigma)$ is related to the cross section of interest, σ, via Eq. (6). The dependencies of N_s^i, $\epsilon_s^{i,j}$, and f_s^i on $t_{\mathcal{L}_{\text{eff}}}$, t_{Q_y}, and LCE are suppressed for clarity. The shapes in cS1, $f_{s,b}$, are considered for each event, k, in the second term of Eq. (13). The background model uncertainties, shown in Fig. 10 (black line), are modeled through variations of $\epsilon_b^{i,j}$, constrained by

$$\mathcal{L}_2^i = \prod_j^{K^i(m_\chi)} \text{Poiss}(m_b^{i,j}|\epsilon_b^{i,j} M_b^i), \quad (14)$$

where M_b^i is the total number of ER calibration events and $m_b^{i,j}$ is the number in each band. The global nuisance parameters $t_{\mathcal{L}_{\text{eff}}}$ and t_{Q_y} are constrained by external light and charge yield measurements through

FIG. 9. Integrated event rates for each PL band assuming a 50 GeV/c^2 WIMP at $\sigma_{\text{SI}} = 10^{-45}$ cm^2 in runs I (top), II (middle), and III (bottom). Banding and legend similar to Fig. 8. The solid line error bars on the total correspond to the total Poisson error defined from ER calibration data shown in Fig. 10, while the dotted lines show the 68% Poisson probability region for the expectation.

The full likelihood for the combination of the three science runs can be written as

$$\mathcal{L} = \mathcal{L}^I \times \mathcal{L}^{II} \times \mathcal{L}^{III} \times \mathcal{L}_3(t_{\mathcal{L}_{\text{eff}}}) \times \mathcal{L}_4(t_{Q_y}), \quad (11)$$

where the likelihood function for a given science run, i, is

TABLE II. Relative contribution (%) of each background component in the ROI.

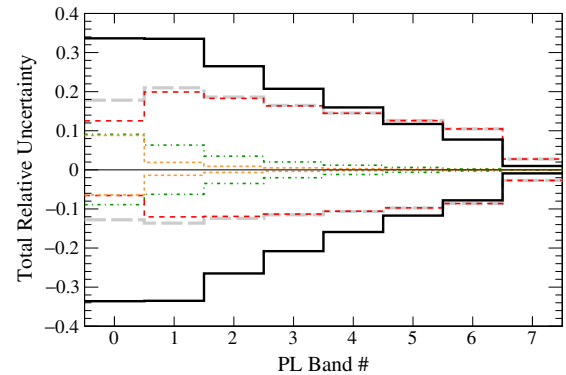|	Run I	Run II	Run III
Gaussian ER	64 ± 6	55 ± 8	72 ± 7
Non-Gaussian ER	33 ± 5	35 ± 7	19 ± 4
NR	3 ± 2	10 ± 7	9 ± 7

FIG. 10. Total uncertainty for each background component and their quadrature sum (long-dashed gray line) in run III. Banding and legend similar to Fig. 8, except for including the Poisson error defined from ER calibration data (solid black line) to visualize the constraint term in Eq. (14). Positive and negative lines show an asymmetric uncertainty.
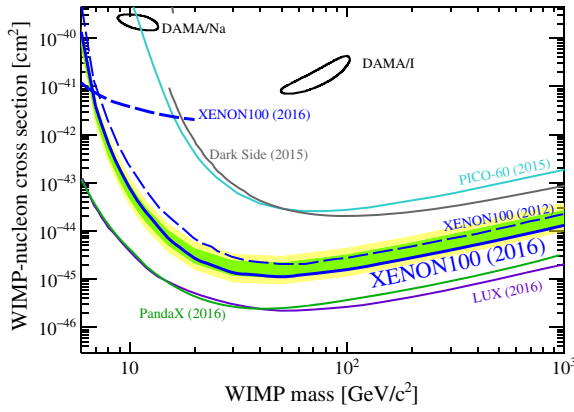
FIG. 11.   Spin-independent cross section limit (blue line) and 1σ (green band) and 2σ (yellow band) expected sensitivity regions at 90% C.L. from the combined analysis of the three XENON100 science runs. For comparison, a subset of other experimental limits (90% C.L.) and detection claims (2σ) are also shown [12,30–35].
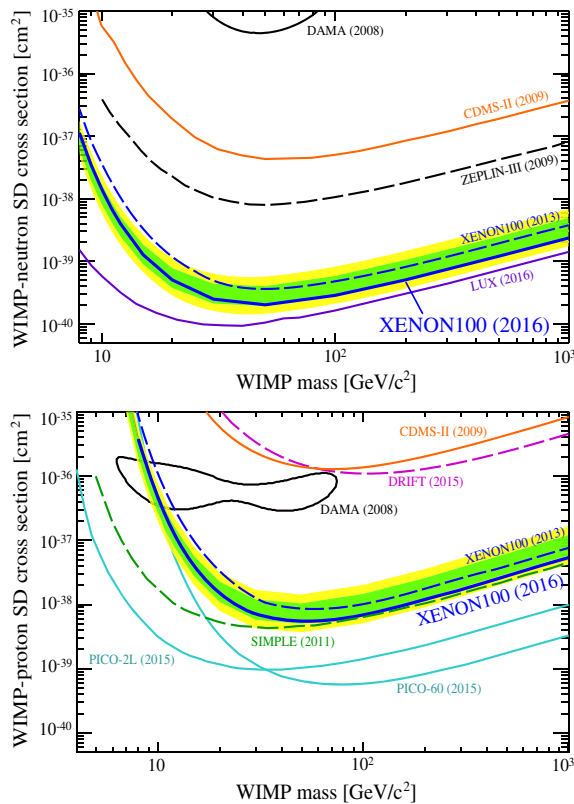

FIG. 12.   Spin-dependent cross section limit (blue line) and 1σ (green band) and 2σ (yellow band) expected sensitivity regions at 90% C.L. from the combined analysis of the three XENON100 science runs. The top (bottom) panel shows the individual neutron (proton) only cross sections. For comparison, other experimental limits (90% C.L.) and detection claims (2σ) are also shown [13,31,36–42].

$$\mathcal{L}_{3,4}(t_{\mathcal{L}_{\mathrm{eff}}}, t_{Q_y}) = \exp(-(t_{\mathcal{L}_{\mathrm{eff}}}, t_{Q_y})^2/2), \qquad (15)$$

with the allowed variation derived from the spread and uncertainties in those data [10].

III. WIMP SEARCH RESULTS

After unblinding the run III ROI, no significant excess of events over the expected background is observed, as shown in Table I and Fig. 9. The PL analysis of the combined data results in a 90% confidence level (C.L.) limit using the CL_s prescription [28] on the WIMP-nucleon SI cross section as shown in Fig. 11, corresponding to 1.1×10^{-45} cm^2 at a 50 GeV/c^2 mass. The green and yellow sensitivity bands represent the distribution of expected upper limits under the assumption of no signal. A cross-check with a second independent PL code using the same inputs, as well as an order of magnitude check with a maximum gap analysis [29], resulted in limits consistent within the sensitivity bands. The XENON100 run III result confirms the absence of a WIMP dark matter signal and a combination of the data improves the limit on the SI WIMP-nucleon cross section by a factor of 1.8 at 50 GeV/c^2 mass compared to the previously published XENON100 limit [12].

We apply the same statistical approach to set upper limits on the SD WIMP-proton and neutron cross sections, shown in Fig. 12. For coupling to protons, the limit at 50 GeV/c^2 is 5.2×10^{-39} cm^2, whereas for neutrons it is 2.0×10^{-40} cm^2. This constitutes improvements by factors of 1.7 and 1.8, respectively, compared to the previously published XENON100 limits [13].

IV. SUMMARY

We present the final XENON100 spin-independent and spin-dependent results from the combined analysis of two already published science runs and a third new run, with a total exposure of 477 live days (48 kg × yr) acquired between January 2010 and January 2014. Improvements to the data quality event selection were described, resulting in a reduction of background and increase in purity of the final dark matter sample. A new technique to quantify accidental coincidences was developed and implemented into the ER background model. Furthermore, the signal model is now computed analytically for S1 and S2, including more accurate modeling of all acceptances and thresholds. Finally, requiring a minimum number of detected signal quanta improves the robustness of the analysis close to the energy threshold, which is important for low WIMP masses. No evidence for dark matter is found and an upper limit of the WIMP-nucleon cross section is derived. The combination of the three science runs with the improved analysis results in a SI limit of 1.1×10^{-45} cm^2 at a 50 GeV/c^2 mass and a SD neutron (proton) limit of 2.0×10^{-40} cm^2 (5.2×10^{-39} cm^2) at 50 GeV/c^2 mass.

ACKNOWLEDGMENTS

APPENDIX: ACCIDENTAL COINCIDENCE BACKGROUND MODEL

A data-driven method to estimate the accidental coincidence (AC) rate was developed, similar to [43]. Lone S2s are selected with the same S2-related criteria, referenced and described in Sec. II C, as well as requiring no S1 preceding the S2 in the event waveform. To derive the lone S1 spectrum, events in the S2-S1 plane are categorized into two regions that are known to consist mostly of ACs: type A events with a large S2 paired with a small S1, and type B events with a very small S2 paired with any S1, as shown in Fig. 13. Type A events are mostly ACs, but are limited to lower S1s and in statistics. Type B events have large statistics across S1, but
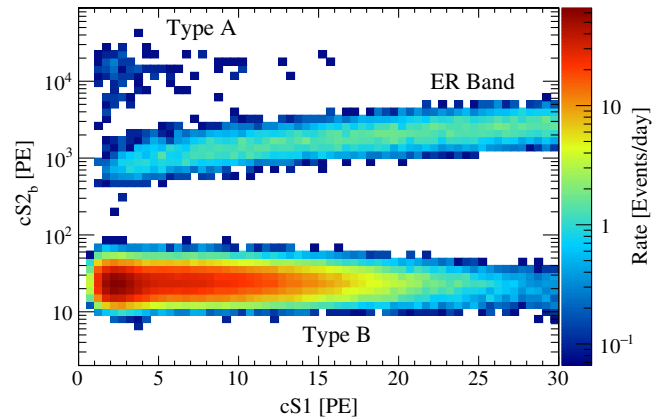

FIG. 13. Event categorization (types A and B) for the accidental coincidence background model. The run III ER calibration data are shown, but are similar for all runs and DM science data.

are contaminated by events where the S2 was caused by the S1 through impurity photoionization S2s. These secondary S2s are modeled by the rate difference between type A and type B events. The lone S1 spectrum is then derived from the type B S1 spectrum after subtracting the secondary S2s. Finally, the AC rate is given by the product of the lone S1 and lone S2 spectra, and is shown in Fig. 7 (middle). The uncertainty, shown in Fig. 10, is dominated by systematic uncertainties from the modeling of the secondary S2s which is limited by type A event statistics.

[1] D. Harvey, R. Massey, T. Kitching, A. Taylor, and E. Tittley, The non-gravitational interactions of dark matter in colliding galaxy clusters, Science **347,** 1462 (2015).

[2] P. A. R. Ade *et al.* (Planck Collaboration), Planck 2015 results. XIII. Cosmological parameters, Astron. Astrophys. **594,** A13 (2016).

[3] G. Jungman, M. Kamionkowski, and K. Griest, Supersymmetric dark matter, Phys. Rep. **267,** 195 (1996).

[4] *Particle Dark Matter*, edited by G. Bertone (Cambridge University Press, Cambridge, England, 2010).

[5] T. Marrodán Undagoitia and L. Rauch, Dark matter direct-detection experiments, J. Phys. G **43,** 013001 (2016).

[6] E. Aprile *et al.* (XENON100 Collaboration), The XENON100 dark matter experiment, Astropart. Phys. **35,** 573 (2012).

[7] E. Aprile *et al.* (XENON100 Collaboration), Material screening and selection for XENON100, Astropart. Phys. **35,** 43 (2011).

[8] E. Aprile *et al.* (XENON100 Collaboration), Study of the electromagnetic background in the XENON100 experiment, Phys. Rev. D **83,** 082001 (2011).

[9] E. Aprile *et al.* (XENON100 Collaboration), The neutron background of the XENON100 dark matter search experiment, J. Phys. G **40,** 115201 (2013).

[10] E. Aprile *et al.* (XENON100 Collaboration), Dark Matter Results from 100 Live Days of XENON100 Data, Phys. Rev. Lett. **107,** 131302 (2011).

[11] E. Aprile *et al.* (XENON100 Collaboration), Implications on inelastic dark matter from 100 live days of XENON100 data, Phys. Rev. D **84,** 061101 (2011).

[12] E. Aprile *et al.* (XENON100 Collaboration), Dark Matter Results from 225 Live Days of XENON100 Data, Phys. Rev. Lett. **109,** 181301 (2012).

[13] E. Aprile *et al.* (XENON100 Collaboration), Limits on Spin-Dependent WIMP-Nucleon Cross Sections from 225 Live Days of XENON100 Data, Phys. Rev. Lett. **111,** 021301 (2013).

[14] E. Aprile *et al.* (XENON100 Collaboration), Analysis of the XENON100 dark matter search data, Astropart. Phys. **54,** 11 (2014).

[15] G. Plante, E. Aprile, R. Budnik, B. Choi, K.-L. Giboni, L. W. Goetzke, R. F. Lang, K. E. Lim, and A. J. Melgarejo Fernandez, New measurement of the scintillation efficiency

of low-energy nuclear recoils in liquid xenon, Phys. Rev. C **84,** 045805 (2011).

[16] E. Aprile, C. E. Dahl, L. de Viveiros, R. J. Gaitskell, K. L. Giboni, J. Kwong, P. Majewski, K. Ni, T. Shutt, and M. Yamashita, Simultaneous Measurement of Ionization and Scintillation from Nuclear Recoils in Liquid Xenon as Target for a Dark Matter Experiment, Phys. Rev. Lett. **97,** 081302 (2006).

[17] E. Aprile *et al.* (XENON100 Collaboration), Response of the XENON100 dark matter detector to nuclear recoils, Phys. Rev. D **88,** 012006 (2013).

[18] E. Aprile *et al.* (XENON100 Collaboration), Observation and applications of single-electron charge signals in the XENON100 experiment, J. Phys. G **41,** 035201 (2014).

[19] S. Lindemann and H. Simgen, Krypton assay in xenon at the ppq level using a gas chromatographic system combined with a mass spectrometer, Eur. Phys. J. C **74,** 2746 (2014).

[20] J. Aalbers and C. Tunnell, The pax data processor v4.0.0, July, 2016, http://dx.doi.org/10.5281/zenodo.58613.

[21] E. Aprile *et al.* (XENON100 Collaboration), Physics reach of the xenon1t dark matter experiment, J. Cosmol. Astropart. Phys. 04 (2016) 027.

[22] J. Lewin and P. Smith, Review of mathematics, numerical factors, and corrections for dark matter experiments based on elastic nuclear recoil, Astropart. Phys. **6,** 87 (1996).

[23] A. M. Green, Astrophysical uncertainties on direct detection experiments, Mod. Phys. Lett. A **27,** 1230004 (2012).

[24] M. C. Smith, G. Ruchti, A. Helmi, R. Wyse, J. Fulbright *et al.*, The RAVE survey: Constraining the local galactic escape speed, Mon. Not. R. Astron. Soc. **379,** 755 (2007).

[25] E. Aprile *et al.* (XENON100 Collaboration), Likelihood approach to the first dark matter results from XENON100, Phys. Rev. D **84,** 052003 (2011).

[26] J. Menéndez, D. Gazit, and A. Schwenk, Spin-dependent WIMP scattering off nuclei, Phys. Rev. D **86,** 103511 (2012).

[27] G. Cowan, K. Cranmer, E. Gross, and O. Vitells, Asymptotic formulae for likelihood-based tests of new physics, Eur. Phys. J. C **71,** 1554 (2011).

[28] A. L. Read, Modified frequentist analysis of search results (The CLs method), in *Proceedings, First Workshop on Confidence Limits*, CERN, Geneva, Switzerland, 17–18 Jan 2000 (CERN-2000-005), 2000, pp. 81–101.

[29] S. Yellin, Some ways of combining optimum interval upper limits, arXiv:1105.2928.

[30] R. Bernabei *et al.* (DAMA Collaboration), First results from DAMA/LIBRA and the combined results with DAMA/NaI, Eur. Phys. J. C **56,** 333 (2008).

[31] C. Amole *et al.* (PICO Collaboration), Dark matter search results from the PICO-60 CF_3I bubble chamber, Phys. Rev. D **93,** 052014 (2016).

[32] E. Aprile *et al.* (XENON100 Collaboration), A low-mass dark matter search using ionization signals in XENON100, Phys. Rev. D **94,** 092001 (2016).

[33] A. Tan *et al.* (PandaX-II Collaboration), Dark Matter Results from First 98.7-Day Data of PandaX-II Experiment, Phys. Rev. Lett. **117,** 121303 (2016).

[34] D. S. Akerib *et al.*, Results from a search for dark matter in LUX with 332 live days of exposure, arXiv:1608.07648.

[35] P. Agnes *et al.* (DarkSide Collaboration), Results from the first use of low radioactivity argon in a dark matter search, Phys. Rev. D **93,** 081101 (2016).

[36] D. S. Akerib *et al.* (LUX Collaboration), First Spin-Dependent WIMP-Nucleon Cross Section Limits from the LUX Experiment, Phys. Rev. Lett. **116,** 161302 (2016).

[37] C. Amole *et al.* (PICO Collaboration), Improved dark matter search results from PICO-2L Run 2, Phys. Rev. D **93,** 061101 (2016).

[38] J. B. R. Battat *et al.* (DRIFT Collaboration), First background-free limit from a directional dark matter experiment: results from a fully fiducialised DRIFT detector, Phys. Dark Univ. **9,** 1 (2014).

[39] R. Bernabei *et al.*, Investigating the DAMA annual modulation data in a mixed coupling framework, Phys. Lett. B **509,** 197 (2001).

[40] V. N. Lebedenko *et al.* (ZEPLIN-III Collaboration), Limits on the Spin-Dependent WIMP-Nucleon Cross-Sections from the First Science Run of the ZEPLIN-III Experiment, Phys. Rev. Lett. **103,** 151302 (2009).

[41] Z. Ahmed *et al.* (CDMS Collaboration), Search for Weakly Interacting Massive Particles with the First Five-Tower Data from the Cryogenic Dark Matter Search at the Soudan Underground Laboratory, Phys. Rev. Lett. **102,** 011301 (2009).

[42] M. Felizardo, T. Girard, T. Morlat, A. Fernandes, A. Ramos *et al.* (SIMPLE Collaboration), Final Analysis and Results of the Phase II SIMPLE Dark Matter Search, Phys. Rev. Lett. **108,** 201302 (2012).

[43] X. Xiao *et al.* (PandaX Collaboration), Low-mass dark matter search results from full exposure of the PandaX-I experiment, Phys. Rev. D **92,** 052004 (2015).